
Article:
Tsiapalis, A. orcid.org/0009-0000-9782-0651, Zsámberger, N.K. orcid.org/0000-0002-2822-129X, Asztalos, B. orcid.org/0000-0001-8530-5855 et al. (1 more author) (2025) Nonparallel wave propagation in an asymmetric magnetic slab. The Astrophysical Journal, 988 (1). 38. ISSN 0004-637X

https://doi.org/10.3847/1538-4357/addc69

The Astrophysical Journal, 988:38 (16pp), 2025 July 20 https://doi.org/10.3847/1538-4357/addc69

Nonparallel Wave Propagation in an Asymmetric Magnetic Slab

Antreas Tsiapalis[1], Noémi Kinga Zsámberger[1,2,3,4], Balázs Asztalos[4,5], and Robert Erdélyi[1,4,5]
[1] Solar Physics and Space Plasma Research Centre, School of Mathematical and Physical Sciences, University of Sheffield, Hicks Building, Hounsfield Road, Sheffield, S3 7RH, UK; robertus@sheffield.ac.uk
[2] Department of Physics, University of Debrecen, 1. Egyetem tér, H-4010, Debrecen, Hungary
[3] Doctoral School of Physics, University of Debrecen, 1. Egyetem tér, Debrecen, H-4010, Hungary
[4] Gyula Bay Zoltán Solar Observatory (GSO), Hungarian Solar Physics Foundation (HSPF), Petőfi tér 3., Gyula, H-5700, Hungary
[5] Department of Astronomy, Eötvös Loránd University, 1/A Pázmány Péter sétány, H-1117 Budapest, Hungary
Received 2024 October 2; revised 2025 May 20; accepted 2025 May 21; published 2025 July 11

Abstract

Theoretical and numerical analyses of the behavior of magnetohydrodynamic (MHD) waves in solar atmospheric structures have a vital role in understanding the plasma dynamics of the Sun. Magneto-helioseismology is indebted to the insight gained from simple magnetic slab structures accompanied by varying conditions within the slab and its environment. This paper builds on the existing literature on these structures by presenting an analytical approach to deriving the dispersion relation for MHD wave propagation in a nonparallel case. Analogous to the parallel case, a plethora of modes emerges that can be classified into quasi-kink or quasi-sausage, body or surface, as well as fast or slow waves. The slab itself can be viewed as thin or wide similarly to previous works, however due to the nonparallel condition it can also be categorised as short or long in the direction of the tilt of the wavevector. This is the analog of the thin or wide slab classification in the parallel direction, expanding our established knowledge regarding propagating MHD waves in magnetic slabs. The variance of the wavenumber along the nonparallel dimension brings to light a number of intriguing features, such as modes changing character with variation of the angle of the wavevector while the propagation speed remains the same. Further new information is provided by the newly derived classification limits, $u_{\pm}$, which act as a form of generalised Alfvén and sound speeds in the dispersion relation.

Unified Astronomy Thesaurus concepts: Solar atmosphere (1477); Solar magnetic fields (1503); Helioseismology (709); Solar physics (1476); Magnetohydrodynamics (1964); Solar coronal waves (1995); Quiet solar corona (1992); Quiet solar chromosphere (1986); Solar oscillations (1515)

Materials only available in the online version of record: animations

1. Introduction

The dynamic activity of our Sun owes its nature to the ubiquitous existence of magnetic fields throughout its atmosphere. The magnetic structuring present at different scales allows for a variety of magnetohydrodynamic (MHD) waves to propagate. At the same time, dynamic solar events have been unanimously recognized as a means of driving perturbations in magnetically dominated regions like the corona (D. Banerjee et al. 2007; J. A. McLaughlin et al. 2011; I. Arregui et al. 2012; M. Mathioudakis et al. 2013; R. Komm et al. 2015). This establishes the importance of rigorously studying wave propagation in magnetic structures as a means of plasma diagnostics.

On top of this, studying the different interactions of MHD waves can grant insight into the mechanisms for coronal heating such as phase mixing (J. Heyvaerts & E. R. Priest 1983) and resonant absorption (M. Goossens et al. 2011).

The structure of a magnetic waveguide can be studied through leveraging the tools of solar magneto-seismology (SMS; see the reviews by V. M. Nakariakov & E. Verwichte 2005; J. Andries et al. 2009; M. S. Ruderman & R. Erdélyi 2009; I. De Moortel & V. M. Nakariakov 2012; R. Erdélyi & N. K. Zsámberger 2024). SMS methods combine theoretical investigations with observational results for MHD wave propagation. These two directions of study are used to compare calculated and measured values for the properties of the waves in order to carry out a meticulous analysis of the MHD waveguide environment (R. J. Morton et al. 2012). This allows certain properties of solar waveguides which would be difficult to measure directly (such as the coronal magnetic field strength) to be estimated indirectly through SMS methods (V. M. Nakariakov & L. Ofman 2001; R. Erdélyi & Y. Taroyan 2008; M. Allcock et al. 2019).

At its core, SMS and space-weather physics start with the investigation of relatively simple magnetic structures, then extend the model for a solar framework by capturing further details of the fundamental physical processes present in solar atmospheric waveguides. By using this step-by-step approach it is possible to build on past results, expand in new directions, and leverage these new results to build a deeper understanding of solar waveguides.

In the earlier stages of investigating linear MHD waves, studies focused on a single interface (B. Roberts 1981a). Then the magnetic and density stratification of the single interface was developed further by considering an isolated slab, where a second interface secluded a plasma region permeated by a straight magnetic field between the two boundary layers, isolating it from the nonmagnetic external regions (B. Roberts 1981b). The magnetic, density, and flow properties of the plasma in the three distinct regions became gradually more complex, from an isolated symmetric magnetic

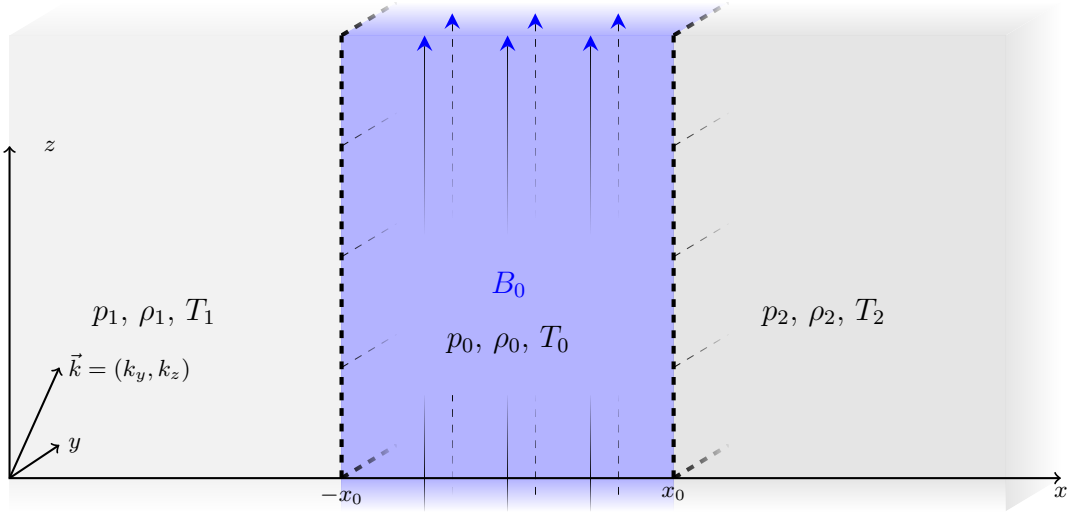

Figure 1. Illustration of a magnetic slab in an asymmetric nonmagnetic environment.

slab to having a uniform magnetic field externally (P. M. Edwin & B. Roberts 1982), or maintaining the isolated magnetic slab but adding a density differential—an asymmetry—to the two external regions (M. Allcock & R. Erdélyi 2017, 2018). The asymmetry was then extended to the magnetic properties of the outside regions, i.e., having two different magnetic fields to the left and right of the slab (N. K. Zsámberger et al. 2018; N. K. Zsámberger & R. Erdélyi 2020).

The investigation of the Cartesian geometry of planar interfaces was continued by adding multiple interfaces, resulting in a complex waveguide model composed of plane-parallel regions with different atmospheric properties, where either only a single region maintained its magnetic structure (D. Shukhobodskaia & R. Erdélyi 2018) or a magnetic differential was added on top of the density stratification to all regions (M. Allcock et al. 2019). Another frequently utilized approach is one that considers the presence of bulk background flows in the plasma, with jet structures formed by velocity fields (V. M. Nakariakov & B. Roberts 1995; M. Barbulescu & R. Erdélyi 2018; N. K. Zsámberger et al. 2022).

Simultaneously, a number of modeling studies adopted cylindrical geometries over Cartesian ones, with significant impact on the development and application of SMS (H. Rosenberg 1970; Y. Uchida 1970; V. V. Zajtsev & A. V. Stepanov 1975; B. Roberts et al. 1984; M. Goossens et al. 2002). The analysis of cylindrical structures seems natural in a solar context as atmospheric magnetic flux-tube oscillations have been widely observed (M. J. Aschwanden et al. 1999; V. M. Nakariakov et al. 1999, 2024; V. M. Nakariakov & E. Verwichte 2005; D. Banerjee et al. 2007, 2021; T. Wang 2011; I. De Moortel & V. M. Nakariakov 2012; B. Roberts 2024), while Cartesian configurations have provided insight into more elongated complex magnetic structures, such as prominences (P. S. Joarder & B. Roberts 1992a, 1992b, 1993; I. Arregui & J. L. Ballester 2011).

The present analysis aims to expand on the aforementioned studies of MHD wave propagation in asymmetric Cartesian waveguides in another direction, in a configuration where the propagation is allowed to be nonparallel or oblique with respect to the magnetic field. Specifically, we study an isolated magnetic slab with an asymmetry of atmospheric properties (density, pressure, temperature), both compared to the inside of the slab and between the left and right environmental regions. As Figure 1 illustrates, this structuring appears along the x-direction, while the system remains infinite in the perpendicular horizontal y-direction and the vertical z-direction. This slab geometry is now examined under the additional condition of nonparallel wave propagation, i.e., $\boldsymbol{k} = (k_y, k_z)$. In previous asymmetric Cartesian waveguide studies, propagation was considered purely parallel to the magnetic field and perpendicular to the lateral stratification. This new approach of considering an oblique wavevector can in the future be applied to all past Cartesian-based studies in order to further explore the kind of complex magnetic features investigated by the purely parallel studies. By allowing the propagation to be oblique, initially with asymmetric isolated magnetic slabs, further insights into slab-like solar waveguides are expected. However, this initial investigation can also eventually open the door for extended studies of multiple slabs with nonparallel propagation, all with different magnetic and atmospheric stratification.

In Section 2 of the present paper, first the derivation of the dispersion relation is covered by retaining the nonparallel wavevector component k_y in the governing equation. Next, analytical solutions of interest—incompressible or low-beta plasma, thin and wide, short and long slab approximations—are derived for all different modes in Section 3. Lastly, numerical solutions are presented for different values of the now nonzero k_y-component in Section 4, before a summary of the most important results is given. We also include Appendices to provide an extended comparison of the numerical solutions with the analytical approximations we derived for different modes.

2. Derivation of the Dispersion Relation

2.1. Basic Structure

In the current section, the geometric and physical properties of the investigated model are described in detail, and the linearized ideal MHD equations along with appropriate boundary conditions at the interfaces are used to obtain the dispersion relation describing oblique MHD wave propagation

in the model. For clarity, the following indices are used throughout:

$$i = \begin{cases} 1, & \text{if } x < -x_0 \\ 0, & \text{if } |x| \leqslant x_0 \\ 2, & \text{if } x > x_0 \end{cases}, \qquad j = \begin{cases} 1, & \text{if } x < -x_0 \\ 2, & \text{if } x > x_0. \end{cases}$$

These are utilized if an equation or parameter requires substituting quantities describing both the slab and the external regions (index i), or only the two environmental regions (index j).

Figure 1 shows the equilibrium structure of the magnetic slab model investigated. The width of the slab is $2x_0$, enclosed between the two black lines, and there is a uniform magnetic field $\boldsymbol{B_0}$ inside the structure, visualized with the straight blue arrows. Outside the slab, a nonmagnetic uniform plasma, with asymmetry in terms of gas pressure p, density ρ, and temperature T at its sides, is considered. The asymmetry between the three regions is also portrayed visually by the use of different shades for each in Figure 1. Effects of gravity are omitted for the sake of simplicity, despite its natural correlation with the density stratification of the solar atmosphere. This omission can be excused when the gravity scale height is large compared to the wavelength, thickness, and length of the slab (due to the nonparallel propagation), such as in the present study.

$$\boldsymbol{B} = \begin{cases} B_0 \boldsymbol{z}, & \text{if } |x| \leqslant x_0 \\ 0, & \text{otherwise} \end{cases}$$

and

$$p,\, \rho = \begin{cases} p_1,\, \rho_1, & \text{if } x < -x_0 \\ p_0,\, \rho_0, & \text{if } |x| \leqslant x_0 \\ p_2,\, \rho_2, & \text{if } x > x_0 \end{cases}.$$

The Alfvén speed is zero outside the slab, i.e., $v_{A1} = v_{A2} = 0$, as there is no magnetic field there. Also, the total pressure in these external regions can be characterized solely by the gas pressure p_i. Within the slab, though, the magnetic pressure, which is generated by the Lorentz force of magnitude $B_0^2/2\mu$, with μ being the magnetic permeability, needs to be accounted for. The total pressure should be continuous everywhere and the ratio of specific heats, γ, is assumed to be constant throughout. Combining this information the following relation can be written:

$$p_1 = p_0 + \frac{B_0^2}{2\mu} = p_2. \tag{1}$$

Expressing this condition using the densities and characteristic speeds describing each region, Equation (1) can be rewritten as

$$\rho_1 c_1^2 = \rho_0 c_0^2 + \frac{1}{2}\gamma \rho_0 v_A^2 = \rho_2 c_2^2. \tag{2}$$

Here, $c_i^2 = \gamma p_i/\rho_i$ is the sound speed in each region, while $v_A^2 = B_0^2/\rho_0\mu$ is the Alfvén speed inside the slab. Note that $k = (k_y, k_z)$ is taken to be oblique or nonparallel relative to the magnetic field. This is the main focus of the paper as explained earlier, and will be the reason for the new results derived below. Finally, the ideal MHD equations govern the interactions of the magnetic field and the plasma within the slab:

$$\frac{\partial \boldsymbol{B}}{\partial t} = \boldsymbol{\nabla} \times (\boldsymbol{v} \times \boldsymbol{B}), \tag{3}$$

$$\frac{\partial \rho}{\partial t} + \rho \boldsymbol{\nabla} \cdot \boldsymbol{v} = 0, \tag{4}$$

$$\frac{d}{dt}\left(\frac{p}{\rho^\gamma}\right) = 0, \tag{5}$$

$$\rho \frac{\partial \boldsymbol{v}}{\partial t} = -\boldsymbol{\nabla} p + (\boldsymbol{\nabla} \times \boldsymbol{B}) \times \boldsymbol{B}/\mu, \tag{6}$$

where the variables $\boldsymbol{v} = (v_x, v_y, v_z)$, $\boldsymbol{B}$, p and ρ are the velocity, magnetic field, atmospheric pressure, and density at time t, respectively. The gas law in the form of $p = k_B \rho T/m$ and the solenoidal condition in magnetic fields, i.e., $\boldsymbol{\nabla} \cdot \boldsymbol{B} = 0$, are also employed.

2.2. Governing Equation

At this point, linearization for small perturbations of the MHD equations is executed. After combining the results, the Fourier components of the system are considered, seeking solutions in the form of

$$\begin{aligned} v_{x,y,z} &= \hat{v}_{x,y,z}(x) e^{i(-\omega t + k_y y + k_z z)}, \\ p &= \hat{p}(x) e^{i(-\omega t + k_y y + k_z z)}, \end{aligned} \tag{7}$$

where k_z, k_y are components of the wavenumber vector, and ω is the angular frequency. This ansatz opens the investigation to waves traveling with any angle in the plane defined by the magnetic field and the dimension y perpendicular to both the field and the stratification. Now, the disturbance of velocity has an amplitude $\hat{v_x}$, which obeys the equation

$$\begin{aligned} &\frac{d}{dx}\left\{\frac{\rho(x)(k_z^2 v_A^2(x) - \omega^2)}{(m^2(x) + k_y^2)}\frac{d\hat{v_x}}{dx}\right\} \\ &-\rho(x)(k_z^2 v_A^2(x) - \omega^2)\hat{v_x} = 0, \end{aligned} \tag{8}$$

where

$$m^2(x) = \frac{(k_z^2 v_A^2(x) - \omega^2)((k_z^2 c^2(x) - \omega^2)}{(v_A^2(x) + c^2(x))(k_z^2 c_T^2(x) - \omega^2)}$$

and

$$c_T^2(x) = \frac{c^2(x) v_A^2(x)}{c^2(x) + v_A^2(x)}.$$

This is our governing equation, and it is an ordinary differential equation (ODE) valid for perturbations inside and outside the slab. This equation is formally identical to its counterpart derived in B. Roberts (1981b), only now the k_y-component will also be retained as being nonzero throughout. Equation (8) has a homogeneous limit,

$$\left\{\frac{d^2\hat{v_x}}{dx^2} - (m^2 + k_y^2)\hat{v_x}\right\}(k_z^2 v_A^2 - \omega^2) = 0, \tag{9}$$

which can be used separately for each of the three regions. Hence, for inside the slab the governing equation is

$$\left\{\frac{d^2\hat{v_x}}{dx^2} - (m_0^2 + k_y^2)\hat{v_x}\right\}(k_z^2 v_A^2(x) - \omega^2) = 0, \quad \text{for } |x| \leqslant x_0 \tag{10}$$

where

$$m_0^2 = \frac{(k_z^2 v_A^2 - \omega^2)(k_z^2 c_0^2 - \omega^2)}{(v_A^2 + c_0^2)(k_z^2 c_T^2 - \omega^2)}$$

and

$$c_T^2 = \frac{c_0^2 v_A^2}{c_0^2 + v_A^2},$$

while the governing equation outside the slab is

$$\frac{d^2\hat{v_x}}{dx^2} - (m_j^2 + k_y^2)\hat{v_x} = 0, \tag{11}$$

where

$$m_j^2 = k_z^2 - \frac{\omega^2}{c_j^2}.$$

2.3. Boundary Conditions

An important boundary condition implies that the case of laterally propagating waves as $x \to \pm\infty$ is not considered. This means that the nonmagnetic regions are supposed to act as "absorbers" of energy for the wave, i.e., the waves are evanescent outside the slab. Thus, $m_1^2,\ m_2^2 > 0$, and $\hat{v_x} \to 0$ as $x \to \pm\infty$.

Considering the boundary condition on the velocity in regions 1 and 2, solutions to differential Equations (10) and (11) governing the velocity can be written as

$$\hat{v_x} = \begin{cases} a_1 e^{(m_1^2+k_y^2)^{\frac{1}{2}}(x+x_0)}, & \text{if } x < -x_0 \\ a_0 \cosh\{(m_0^2 + k_y^2)^{\frac{1}{2}}x\} & \\ +b_0 \sinh\{(m_0^2 + k_y^2)^{\frac{1}{2}}x\}, & \text{if } |x| \leqslant x_0 \\ a_2 e^{-(m_2^2+k_y^2)^{\frac{1}{2}}(x-x_0)}, & \text{if } x > x_0 \end{cases}, \tag{12}$$

where a_0, a_1, a_2 and b_0 are all arbitrary constants. The boundary condition carried from the previous argument applies here too:

$$\begin{aligned} m_j^2 + k_y^2 > 0 \ &\Rightarrow \ k_y^2 + k_z^2 - \omega^2/c_j^2 > 0 \\ &\Rightarrow \ \omega^2 < k^2 c_j^2, \end{aligned} \tag{13}$$

while $m_0^2 + k_y^2$ can be negative. These limitations also relate to the ability of the respective regions to support the propagation of surface and/or body waves.

2.4. Continuity Equations

The velocity derivative with respect to the spatial component $d\hat{v_x}/dx$ is easily derived from Equation (12):

$$\frac{d\hat{v_x}}{dx} = \begin{cases} a_1\mu_1 e^{\mu_1(x+x_0)}, & \text{if } x < -x_0 \\ a_0\mu_0 sh_0 + b_0\mu_0 ch_0, & \text{if } |x| \leqslant x_0\,, \\ -a_2\mu_2 e^{-\mu_2(x-x_0)}, & \text{if } x > x_0 \end{cases} \tag{14}$$

where

$$\mu_i = \sqrt{m_i^2 + k_y^2}, \tag{15}$$

and $\mathrm{sh}_0 = \sinh(\mu_0 x_0)$, $\mathrm{ch}_0 = \cosh(\mu_0 x_0)$. It is important that μ_i is not confused with μ, the magnetic permeability. The distinction should be easy through context and the use of indices. Using the linearized MHD equations from earlier, the Fourier form in Equation (7), the magnitude of the total pressure perturbation can be written as

$$\hat{p}_T = d\hat{v_x}/dx \begin{cases} \frac{\Lambda_1}{\mu_1}, & \text{if } x < -x_0, \\ \frac{\Lambda_0}{\mu_0}, & \text{if } |x| \leqslant x_0, \\ \frac{\Lambda_2}{\mu_2}, & \text{if } x > x_0. \end{cases} \tag{16}$$

Here,

$$\begin{aligned} \Lambda_0 &= -\frac{i\rho_0(k_z^2 v_A^2 - \omega^2)}{\mu_0\omega}, \\ \Lambda_j &= \frac{i\rho_j\omega}{\mu_j}. \end{aligned} \tag{17}$$

Applying the continuity condition for velocity and total pressure perturbations, respectively, on the surfaces at $\pm x_0$ in Equations (12) and (16), the following continuity equations emerge:

$$a_1 - a_0 ch_0 + b_0 sh_0 = 0, \tag{18}$$

$$a_0 ch_0 + b_0 sh_0 - a_2 = 0, \tag{19}$$

$$a_1\Lambda_1 + a_0\Lambda_0 sh_0 - b_0\Lambda_0 ch_0 = 0, \tag{20}$$

$$a_0\Lambda_0 sh_0 + b_0\Lambda_0 ch_0 + a_2\Lambda_2 = 0, \tag{21}$$

where a_0, b_0, a_1, a_2 are arbitrary constants as stated earlier.

2.5. Dispersion Relation

Equations (18)–(21) are four equations with four unknowns, a_0, b_0, a_1, and a_2. The following four-by-four matrix of coefficients can be formed, for which the determinant is required to be zero in order to have nontrivial solutions to the system:

$$\begin{bmatrix} 1 & -ch_0 & sh_0 & 0 \\ 0 & ch_0 & sh_0 & -1 \\ \Lambda_1 & \Lambda_0 sh_0 & -\Lambda_0 ch_0 & 0 \\ 0 & \Lambda_0 sh_0 & \Lambda_0 ch_0 & \Lambda_2 \end{bmatrix}, \tag{22}$$

where each row represents one of the continuity equations and each column is the coefficient of one of the four unknowns in that equation, in order a_1, a_0, b_0, a_2. Through a series of algebraic transformations, we arrive at the following quadratic

equation for ω^2:

$$\omega^4 - \frac{1}{2}\frac{\rho_0}{\mu_0}\left(\frac{\mu_1}{\rho_1} + \frac{\mu_2}{\rho_2}\right)(k_z^2 v_A^2 - \omega^2)(th_0 + ct_0)\omega^2 + \frac{\rho_0^2}{\mu_0^2}\frac{\mu_1\mu_2}{\rho_1\rho_2}(k_z^2 v_A^2 - \omega^2)^2 = 0, \quad (23)$$

where $th_0 = sh_0/ch_0 = \tanh \mu_0 x_0$ and $ct_0 = ch_0/sh_0 = \coth \mu_0 x_0$. We note that letting $k_y = 0$, then $\mu_i = m_i$, and the dispersion relation for the case of parallel propagation, Equation (20) in M. Allcock & R. Erdélyi (2017) for an asymmetric slab, can be recovered.

A further similarity to this and other previous asymmetric slab studies (M. Allcock & R. Erdélyi 2017, 2018; N. K. Zsámberger et al. 2018, 2022; D. Shukhobodskaia & R. Erdélyi 2018; M. Allcock et al. 2019; N. K. Zsámberger & R. Erdélyi 2020) is that Equation (23) is a single relation that describes the dispersion of all the eigenmodes propagating obliquely in an asymmetric magnetic slab, which, in the general case, does not decouple into two separate equations describing sausage- or kink-type eigenmodes only. The eigenmodes of these asymmetric slabs possess a mixed character (see, e.g., M. Allcock & R. Erdélyi 2017; N. K. Zsámberger et al. 2018 for details), and following the nomenclature of the preceding asymmetric slab studies listed, we refer to them as quasi-sausage and quasi-kink modes.

2.6. Nonparallel Asymmetric Eigenmodes

Now that a dispersion relation analogous to those of previously studied asymmetric slab systems has been obtained in the form of Equation (23), with certain further assumptions this equation can be decoupled and the standard representation for a dispersion relation in the isolated slab will emerge. Assuming that the physical properties of the two regions outside the slab are of similar scale, the following approximation can be made:

$$\frac{\rho_0}{\mu_0}\frac{\mu_1}{\rho_1} \approx \frac{\rho_0}{\mu_0}\frac{\mu_2}{\rho_2} \approx \frac{1}{2}\frac{\rho_0}{\mu_0}\left(\frac{\mu_1}{\rho_1} + \frac{\mu_2}{\rho_2}\right).$$

Using this so-called weak asymmetry approximation, Equation (23) can be factorized into

$$\{\omega^2 + \Lambda \tanh \mu_0 x_0\}\{\omega^2 + \Lambda \coth \mu_0 x_0\} = 0. \quad (24)$$

Finally, substituting the expressions for Λ from Equation (17) into the factors of this expression leads to the following decoupled dispersion relation:

$$(k_z^2 v_A^2 - \omega^2)\left(\frac{\rho_0}{\rho_1}\mu_1 + \frac{\rho_0}{\rho_2}\mu_2\right) = 2\mu_0\omega^2\begin{bmatrix}\tanh\\ \coth\end{bmatrix}\mu_0 x_0. \quad (25)$$

Throughout the rest of this paper, this will be the form used as the dispersion relation of the system. This equation describes the two types of eigenmodes separately, with the top $\tanh(\mu_0 x_0)$ line representing quasi-sausage modes, and the bottom $\coth(\mu_0 x_0)$ governing quasi-kink modes, both of which are now allowed to have nonparallel propagation.

These waves can be further categorized as surface or body modes. To implement this second type of categorization, the allowed values of μ_0 need to be examined. Consequently, an analysis of the sign of μ_0^2 reveals the intervals of real or complex values of μ_0. Ultimately, positive μ_0^2 corresponds to surface waves, while negative μ_0^2 means body waves. From Equation (15), μ_0^2 can be expanded as

$$\mu_0^2 = \frac{\omega^4 - (k_z^2 + k_y^2)(c_0^2 + v_A^2)\omega^2 + (k_z^2 + k_y^2)k_z^2 c_0^2 v_A^2}{(k_z^2 c_T^2 - \omega^2)(c_0^2 + v_A^2)}. \quad (26)$$

Factorizing the numerator leads to the following, more concise definition composed of only products of two terms both in the numerator and the denominator:

$$\mu_0^2 = \frac{(k^2 u_-^2 - \omega^2)(k^2 u_+^2 - \omega^2)}{(k_z^2 c_T^2 - \omega^2)(c_0^2 + v_A^2)}, \quad (27)$$

where $k^2 = k_z^2 + k_y^2$. The boundaries for classification into body and surface modes will be determined by the new speeds introduced in Equation (27) above, u_- and u_+, which are defined as

$$u_-^2 = \frac{1}{2}(c_0^2 + v_A^2)(1 - A),$$
$$u_+^2 = \frac{1}{2}(c_0^2 + v_A^2)(1 + A),$$
$$\text{and} \quad A^2 = 1 - \frac{4k_z^2 c_T^2}{k^2(c_0^2 + v_A^2)}. \quad (28)$$

Before moving on to classification, the new speeds need to be examined for their properties, i.e., allowed values, real or complex. Starting from the statement below, which is always true for real numbers:

$$k_z^2(c_0^2 - v_A^2)^2 + k_y^2(c_0^2 + v_A^2)^2 \geqslant 0, \quad (29)$$

the following inequality is constructed:

$$(k_z^2 + k_y^2)(c_0^2 + v_A^2)^2 \geqslant 4k_z^2 c_0^2 v_A^2, \quad (30)$$

which, due to the squares present on both sides, compares positive real numbers. Introducing the definition of c_T^2 results in

$$1 \geqslant \frac{4k_z^2 c_T^2}{(k_z^2 + k_y^2)(c_0^2 + v_A^2)}. \quad (31)$$

This means that A, whose square is defined by Equation (28), is also real and positive. Moreover, it can be shown that $0 \leqslant A \leqslant 1$. Therefore, $u_\pm^2 \in \mathbb{R}$ and $u_\pm^2 \geqslant 0$. Having established that $u_\pm^2$ are real and positive, now an assessment as to where the new classification frequencies, $k^2 u_\pm^2$, lie in comparison to $k_z^2 c_T^2$ is needed. This is carried out by rearranging the definition of $u_\pm^2$ from Equation (28) to express $k_z^2 c_T^2$ as

$$k_z^2 c_T^2 = k^2 u_\pm^2\left(1 - \frac{u_\pm^2}{c_0^2 + v_A^2}\right). \quad (32)$$

Now, let us assume that

$$1 - \frac{u_\pm^2}{c_0^2 + v_A^2} > 1. \quad (33)$$

However, this would mean that

$$\frac{u_{\pm}^2}{c_0^2 + v_A^2} < 0, \tag{34}$$

which is invalid, as all components are nonnegative. Hence, $1 - u_{\pm}^2/(c_0^2 + v_A^2) \leqslant 1$ by contradiction, and therefore $k_z^2 c_T^2 \leqslant k^2 u_{\pm}^2$. Now, obviously $u_-^2 \leqslant u_+^2$, so the final ordering of frequencies where the classification between body and surface modes changes is

$$k_z^2 c_T^2 \leqslant k^2 u_-^2 \leqslant k^2 u_+^2. \tag{35}$$

The details of the classification of waves into surface and body modes therefore can be given as follows:

1. Slow surface waves, when $\omega^2 \leqslant k_z^2 c_T^2$.
2. Fast surface waves, for $k^2 u_-^2 \leqslant \omega^2 \leqslant k^2 u_+^2$.
3. Slow body waves, for $k_z^2 c_T^2 \leqslant \omega^2 \leqslant k^2 u_-^2$.
4. Fast body waves, for $k^2 u_+^2 \leqslant \omega^2$.

Note that taking $k_y = 0$ in the definition of $u_{\pm}^2$ results in $u_-^2 = \min(c_0^2, v_A^2)$ and $u_+^2 = \max(c_0^2, v_A^2)$, which reduces μ_0 to m_0 in Equation (25) as expected.

3. Analytical Solutions

After deriving the dispersion relation and establishing the classification of the different eigenmodes that can be guided by this asymmetric slab system, we conducted a further analytical and numerical study of the solutions. First, in the current section, analytical solutions to Equation (25) are provided by analyzing popular, practical limiting cases, i.e., the incompressible, low-beta, thin-short slab, and wide/long slab approximations. This is preceded by briefly addressing leaky and spurious solutions, which limit the allowed values of frequency ω to the trapped solutions. While the analytical work was carried out in conjunction with the numerical investigation, Section 3 focuses on the analytical results, with a separate Section 4 dedicated to numerical results.

3.1. Trapped Solutions

Equation (13) shows that trapped solutions exist for $\omega^2 < k^2 c_j^2$. For nonzero k_y, the governing Equation (9) depends on μ_0, instead of m_0 like in the parallel case. As a result, $k_z c_0$ is no longer a spurious solution for the $k_y \neq 0$ case, while $k_z c_T$ remains one regardless of k_y. In addition, $k_z u_A$ is not only a spurious solution for k_y nonzero, but it is a solution to the governing Equation (9). However, ku_-, ku_+ are now spurious solutions, as they eliminate μ_0 and reduce the governing equation to one with a linear solution, i.e., no wave propagation is permitted.

3.2. Incompressible Limit

In order to adhere to incompressibility, the adiabatic index, γ, and with it the sound speed must become unbounded., i.e., γ, $c_s \to \infty$. As a result, the tube speed, c_T, reduces to the Alfvén speed, v_A, and so m_i^2 reduces to k_z^2. Hence, $\mu_i = (k_z^2 + k_y^2)^{\frac{1}{2}} = k$. This allows us to write Equation (25) as

$$\sigma(k_z^2 v_A^2 - \omega^2) = \omega^2, \tag{36}$$

where

$$\sigma = \frac{1}{2}\left(\frac{\rho_0}{\rho_1} + \frac{\rho_0}{\rho_2}\right)\begin{bmatrix}\tanh\\ \coth\end{bmatrix} kx_0. \tag{37}$$

The solutions in the incompressible limit can then be expressed as

$$\omega^2 = \frac{\sigma}{1+\sigma} k_z^2 v_A^2. \tag{38}$$

As $\sigma \geqslant 0$, therefore $\sigma/(1+\sigma) < 1$. As a result, the incompressible approximation returns sub-Alfvénic phase speeds, which is in agreement with the findings of M. Allcock & R. Erdélyi (2017) for the case of parallel propagation.

3.3. Low-beta Approximation

The low-plasma-β condition is the result of the magnetic pressure dominating the gas pressure inside the slab, i.e., $\beta \coloneqq 2\mu p/B^2 << 1$ (where μ in this case is the magnetic permeability and not the modified m_0 used elsewhere in this paper). This condition translates to the Alfvén speed dominating the sound speed, i.e., $c_0^2/v_A^2 \approx 0$.

To proceed in this limit, the numerical investigation (further described in Section 4) could be utilized, as it showed that the frequencies of propagating waves in this approximation obey $\omega^2 << k_z^2 v_A^2$. In this case, $m_0^2 \approx k_z^2$ and so $\mu_0^2 \approx k^2$. This limits the modes to surface ones as $\mu_0^2 > 0$. However, outside the slab, $\mu_j = (k^2 c_j^2 - \omega^2)^{\frac{1}{2}}/c_j$. Additionally, with such an ordering of the characteristic speeds, the ratios of the internal density to the external ones shown in Equation (2) simplify to

$$\frac{\rho_0}{\rho_j} = \frac{2c_j^2}{\gamma v_A^2}. \tag{39}$$

The low-β condition is a good approximation of the solar coronal environment, but future studies building on this first approximation should ideally incorporate magnetic structures outside the slab.

Considering the full asymmetric system, even with the simplification process detailed above, the dispersion relation can only be transformed into a quadratic equation in ω^2. Instead, here we continue the investigation of M. Allcock & R. Erdélyi (2017), focusing on the solutions when the low-β slab is surrounded by a symmetric environment, but extending their results to the case of allowing nonparallel propagation as well. In this case, the dispersion relation becomes only quadratic in ω^2, with solutions in the following form:

$$\omega^2 = k_z^2 c_e^2 \left\{ \frac{-1 \pm \left(1 + \gamma^2 \frac{k^4}{k_z^4}\begin{bmatrix}\tanh^2\\ \coth^2\end{bmatrix} kx_0\right)^{\frac{1}{2}}}{\frac{1}{2}\gamma^2 \frac{k^2}{k_z^2}\begin{bmatrix}\tanh^2\\ \coth^2\end{bmatrix} kx_0} \right\}. \tag{40}$$

Neglecting the leaky solution and simplifying the remaining components result in the following equation that describes the obliquely propagating wave modes of this symmetric, low-β

magnetic slab:

$$\omega^2 = \frac{2k_z^4 c_e^2}{\gamma^2 k^2}\begin{bmatrix}\coth^2\\ \tanh^2\end{bmatrix}kx_0 \times\left[\left(1+\gamma^2\frac{k^4}{k_z^4}\begin{bmatrix}\tanh^2\\ \coth^2\end{bmatrix}kx_0\right)^{\frac{1}{2}}-1\right]. \quad (41)$$

This pair of equations represents a quasi-sausage (top line) and a quasi-kink (bottom line) surface mode solution to the dispersion relation. A further study of this equation in limiting cases as well as a numerical exploration of the solutions show that for small values of $k_y x_0$ (see also in Section 3.4), both of these solutions tend to the same intermediate frequency as ever wider slabs are considered ($k_z x_0$ increases). In a thin slab ($k_z x_0$ small), the quasi-kink mode tends to a frequency of $\omega = 0$, while the quasi-sausage mode approaches the separation frequency defined above (but now $s_1 = s_2 = s_e$ due to the symmetric sound speeds).

The behavior of the solutions in thin slabs changes as $k_y x_0$ increases, with the quasi-kink mode's frequency increasing, and the quasi-sausage mode's frequency first increasing but then decreasing when $k_z x_0 \to 0$. However, when $k_z x_0$ is also large, the change in the frequencies of both types of waves becomes barely noticeable. Such dependencies on the dimensionless slab width and length are further explored in the next section for the general case (without the restriction of the low-β condition).

3.4. Thin and Wide Slab

The limiting cases of thin/slender and wide slabs have been explored thoroughly in inspiring papers, such as B. Roberts (1981b). The typical methodology consists of considering the relative size of wavelength along the z-axis, $\lambda_z = 2\pi/k_z$ and the width of the slab, x_0. The case when the wavelength is much greater than the width of the slab, i.e., $x_0/\lambda_z = k_z x_0/2\pi << 1$, is referred to as the thin slab. The case when the wavelength is negligible relative to the width of the slab, i.e., $x_0/\lambda_z = k_z x_0/2\pi >> 1$, is referred to as the wide slab. Once again, an extensive analysis of these cases can be found in M. Allcock & R. Erdélyi (2017) for the asymmetric slab, where propagation is considered purely parallel. The present analysis is concerned with the implication of the nonzero wavelength in the y-direction.

Before proceeding to describe the solutions in these traditional applicable limiting cases, similar approximations have to be defined with regard to propagation in the y-direction, too, using the characterizations short slab for $x_0/\lambda_y = k_y x_0/2\pi << 1$ and long slab for $x_0/\lambda_y = k_y x_0/2\pi >> 1$. These are used to identify and describe cases where further analytical conclusions about the obliquely propagating waves can be drawn.

3.4.1. Thin-short Slab

The thin-short slab received the most attention of the four emerging subcases, as it allowed for a more in-depth analysis and the most diverse results. The thin-short slab is defined when both $k_z x_0/2\pi << 1$ and $k_y x_0/2\pi << 1$, i.e., the wavelengths of propagating waves in both dimensions perpendicular to the field are much greater than the lateral dimension of the slab, x_0.

Surface modes. First, let us discuss quasi-sausage modes in the thin-short slab approximation, governed by the tanh version of Equation (25). For surface modes, the simplification $\tanh(\mu_0 x_0) \to \mu_0 x_0$ as $k_z x_0$, $k_y x_0 \to 0$ can be made. This is based on the proof for $m_0 \to 0$ as $k_z x_0 \to$ made in B. Roberts (1981b). The dispersion relation in this case simplifies to

$$(k_z^2 v_A^2 - \omega^2)\left(\frac{\rho_0}{\rho_1}\mu_1 + \frac{\rho_0}{\rho_2}\mu_2\right) = 2\mu_0^2\omega^2 x_0. \quad (42)$$

An inspection of numerical solutions to the dispersion relation (Equation (25)) reveals that in a thin-short slab, slow surface quasi-sausage modes behave like $\omega^2 \to k_z^2 c_T^2$. The form $\omega^2 = k_z^2 c_T^2(1-\nu)$ for some $\nu > 0$ is assumed and substituted into Equation (42) to obtain the following solution:

$$\omega^2 = k_z^2 c_T^2\left[1 - \frac{2(k^2u_-^2 - k_z^2 c_T^2)(k^2 u_+^2 - k_z^2 c_T^2)k_z x_0}{k_z^3(\Gamma_1+\Gamma_2)(v_A^2 - c_T^2)(c_0^2 + v_A^2)}\right], \quad (43)$$

valid for $(1 + k_y^2 + k_z^2)\min(c_1, c_2) > c_T$, where

$$\Gamma_j = \frac{\rho_0}{\rho_j c_j}(k^2 c_j^2 - k_z^2 c_T^2)^{\frac{1}{2}}.$$

Similarly to the case of purely parallel propagation, this equation describes waves that approach the frequency $k_z^2 c_T^2$ from below as $k_z x_0 \to 0$; however, the presence of a k_y-component also influences the exact shape of this solution curve, as we will also show in Section 4.

A noteworthy case appears if a symmetric environment is assumed, i.e., $c_1 = c_2 = c_e$ and $\rho_1 = \rho_2 = \rho_e$. For fast surface quasi-sausage modes in a thin-short slab, it may be assumed that these waves approach the now common external sound speed: $\omega^2 \to k^2 c_e^2$. Under these assumptions, the following equation is derived:

$$\omega^2 = c_e^2[k^2 - k_z^2\lambda^2(k_z x_0)^2], \quad (44)$$

where

$$\lambda = \frac{\rho_e}{\rho_0}\frac{c_e^2(k^2u_-^2 - k_z^2 c_e^2)(k^2u_+^2 - k_z^2 c_e^2)}{k_z^4(c_T^2 - c_e^2)(v_A^2 - c_e^2)(c_0^2 + v_A^2)}.$$

While for very small $k_z x_0$ values, this approximation unfortunately does not capture the sudden decrease in phase speed and deviation from the external sound speed and the related separation speed that the full solutions show, from small to intermediate $k_z x_0$ values, the approximate and exact solution curves are both qualitatively and quantitatively very similar (see also Figure 7 in Appendix B and its accompanying video).

A brief description of quasi-kink surface modes also becomes possible in a thin and short slab. In general, these modes are governed by the coth version of Equation (25). The simplification introduced by assuming that the slab is thin and short allows us to make the substitution $\coth(\mu_0 x_0) \to 1/\mu_0 x_0$, leading to the following solution:

$$\omega^2 = \frac{1}{2}k_z^2 v_A^2\left(\frac{\rho_0}{\rho_1} + \frac{\rho_0}{\rho_2}\right)kx_0. \quad (45)$$

This type of solution shows a much clearer influence of the oblique propagation, with a linear dependence on both wavenumber components contained in the final kx_0 term.

We also note the absence of a companion quasi-kink mode to the quasi-sausage mode of Equation (45). This is because fast quasi-kink surface modes, when they are present, show a more complex behavior. As P. M. Edwin & B. Roberts (1982) noted in the case of symmetric slabs, these solutions to the dispersion relation enter the band of surface modes delineated by the characteristic speeds of the system only at an intermediate slab width (in the z-direction, and as $k_z x_0$ decreases, the solution curve continues in a band of body modes). We have also recovered this behavior, however we make further observations on this mode as we describe the results of our numerical investigation in Section 4.

Body modes. The simplifications to describe the quasi-kink and quasi-sausage surface modes above were made under the assumption of $\mu_0 > 0$. This does not exhaust all possible modes. The case of μ_0 remaining bounded while $k_z x_0, k_y x_0 \to 0$ has also to be considered. That is achievable only for $\mu_0 < 0$, specifically for $\omega \to k_z c_T$ as $k_z x_0, k_y x_0 \to 0$, i.e., body waves. For slow body modes, which approach the tube speed in thin slabs, the form $\omega^2 = k_z^2 c_T^2(1 - \nu(kx_0)^2)$ (with ν to be determined) is used, as it satisfies the requirements above. As a result, the slow quasi-sausage body modes in a thin-short slab are given as a countably infinite set for $\nu = \nu_n$ that behave like

$$\omega_n^2 = k_z^2 c_T^2\left(1 + \frac{(k^2u_-^2 - k_z^2c_T^2)(k^2u_+^2 - k_z^2c_T^2)}{k_z^4u_-^2u_+^2\pi^2n^2}(k_z x_0)^2\right),$$
$$n = 1, 2,\ldots. \tag{46}$$

Similarly, the slow quasi-kink body modes in a thin-short slab are also a countably infinite set that are slightly faster and behave like

$$\omega_n^2 = k_z^2 c_T^2\left(1 + \frac{(k^2u_-^2 - k_z^2c_T^2)(k^2u_+^2 - k_z^2c_T^2)}{k_z^4u_-^2u_+^2\pi^2\left(n - \frac{1}{2}\right)^2}(k_z x_0)^2\right),$$
$$n = 1, 2,\ldots. \tag{47}$$

3.4.2. Wide and/or Long Slab

The wide and long characterization of the slab refer to $k_z x_0 >> 1$ and $k_y x_0 >> 1$, respectively. Therefore, unlike in the case of the thin-short slab examined above, at least one wavelength, either λ_z or λ_y, will be much smaller than the lateral dimension. These are the wide-short, thin-long, and wide-long subcases. In any of these scenarios, the same simplification can be made, due to the fact that $\mu_0 x_0 = (m_0^2x_0^2 + k_y^2x_0^2)^{\frac{1}{2}} >> 1$ if $m_0 x_0 >> 1$ and/or $k_y x_0 >> 1$. The latter is self-explanatory, while the first is proven for the case of $k_z x_0 >> 1$ in B. Roberts (1981b). The simplification that can be made in this case is that both $\tanh(\mu_0 x_0) \approx 1$ and $\coth(\mu_0 x_0) \approx 1$ when $\mu_0 x_0 >> 1$. This reduces the dispersion relation to

$$(k_z^2v_A^2 - \omega^2)\left(\frac{\rho_0}{\rho_1}\mu_1 + \frac{\rho_0}{\rho_2}\mu_2\right) = 2\mu_0\omega^2. \tag{48}$$

This is formally equivalent to the single-interface problem with modified density ratios and wavenumber. It is k_y dependent but not to a degree that induces any qualitative change to the solution.

The body modes, however, do not have a parallel in the single-interface problem, as they owe their existence to the barriers and are externally evanescent. Under the wide and/or long slab conditions there exists a solution for $\omega^2 \to k^2u_-^2$ as $\mu_0 x_0 \to \infty$. To show this, we substitute the ansatz $\omega^2 = k^2u_-^2(1 + \nu/(kx_0)^2)$ into the dispersion relation to retrieve two countably infinite solution sets, given by

$$\omega_n^2 = k^2u_-^2\left(1 - \frac{\pi^2\left(n - \frac{1}{2}\right)^2(k^2u_-^2 - k_z^2c_T^2)(c_0^2 + v_A^2)}{k^2u_-^2(u_+^2 - u_-^2)(kx_0)^2}\right),$$
$$n = 1, 2, \ldots \tag{49}$$

for quasi-sausage modes and similarly,

$$\omega_n^2 = k^2u_-^2\left(1 - \frac{\pi^2n^2(k^2u_-^2 - k_z^2c_T^2)(c_0^2 + v_A^2)}{k^2u_-^2(u_+^2 - u_-^2)(kx_0)^2}\right),$$
$$n = 1, 2, \ldots \tag{50}$$

for quasi-kink modes.

Unlike the parallel case, the ordering of c_0 and v_A does not change the solutions, since the ordering of u_- and u_+ is absolute.

Using a similar approach to retrieve an approximation for fast body modes from the decoupled dispersion relation, we see that another two sets of countably infinite solutions exist in the wide and/or long slab. Specifically, the ansatz $\omega^2 = k^2u_+^2(1 + \nu/(kx_0)^2)$ yields

$$\omega_n^2 = k^2u_+^2\left(1 + \frac{\pi^2\left(n - \frac{1}{2}\right)^2(k^2u_+^2 - k_z^2c_T^2)(c_0^2 + v_A^2)}{k^2u_+^2(u_+^2 - u_-^2)(kx_0)^2}\right),$$
$$n = 1, 2, \ldots \tag{51}$$

for quasi-sausage fast body modes and similarly,

$$\omega_n^2 = k^2u_+^2\left(1 + \frac{\pi^2n^2(k^2u_+^2 - k_z^2c_T^2)(c_0^2 + v_A^2)}{k^2u_+^2(u_+^2 - u_-^2)(kx_0)^2}\right),$$
$$n = 1, 2, \ldots \tag{52}$$

for quasi-kink fast body modes. These are both solutions that approach the higher one of the classification speeds, u_+, from above as the slab becomes wider or longer. This can coincide with an increase in the phase speed of the solutions at identical slab widths but longer slab lengths, as the classification speeds themselves also depend on the slab length (as mentioned above).

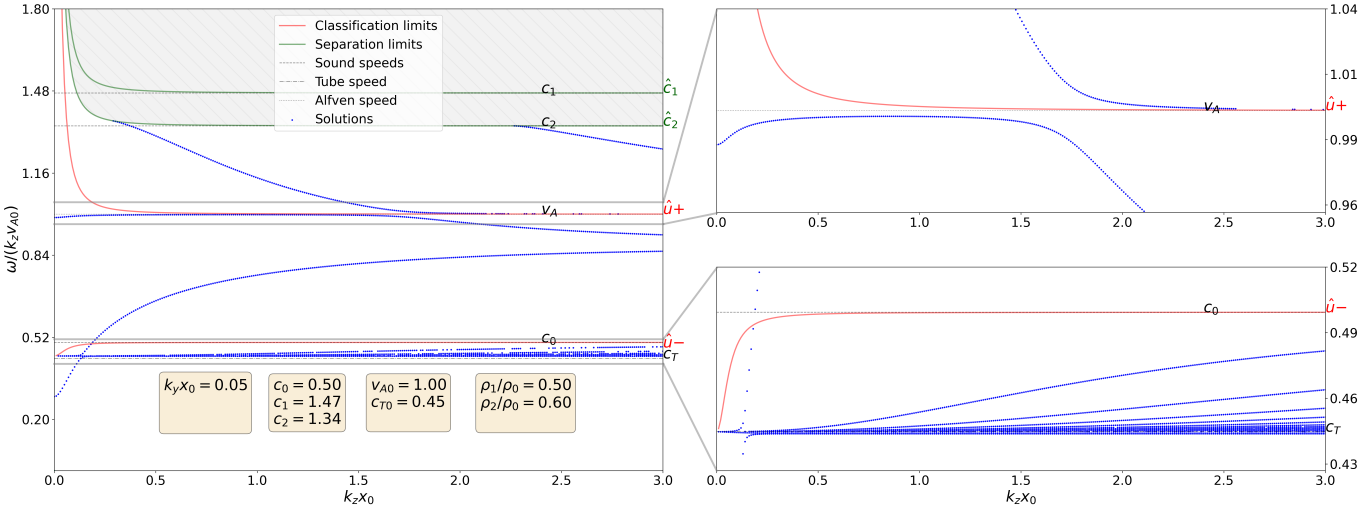

(a) Solutions in a short slab ($k_y x_0 = 0.05$)

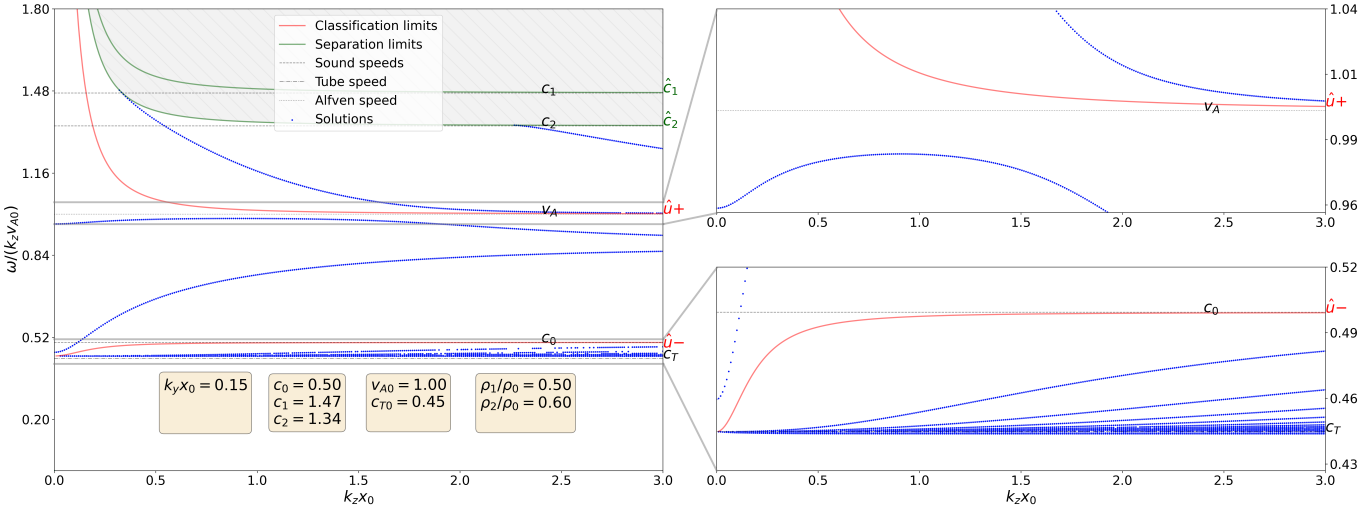

(b) Solutions in a longer slab ($k_y x_0 = 0.15$)

Figure 2. The normalized phase speed as a function of slab width for a short (top) and a longer (bottom) slab, and areas of interest enlarged in the right-hand-side panels of each diagram. An animation of this figure is available, where each frame shows a slab of different lengths between $0 \leqslant k_y x_0 \leqslant 0.4$, changing with an increment of $k_y x_0 = 0.05$ between frames.

(An animation of this figure is available in the online article.)

4. Numerical Solutions

In this section, the dispersion relation is solved numerically with greater focus given to the changes induced by the k_y-variation and by characterization of the slab into long and short.

Consider an asymmetric magnetic slab as a base, for which the equilibrium conditions are given in Figure 2 and explored in Section 2. For that slab, allow the propagation to take place nonparallel, including a k_y-component in the wavevector $\boldsymbol{k}$. The general dispersion relation for these circumstances is given by Equation (23). Note that the solution does not decouple into two distinct solutions, typically referred to as sausage for the tanh version, and kink for the coth one. Instead, they appear coupled, similar to what was found in M. Allcock & R. Erdélyi (2017) for the parallel slab, i.e., the subcase of Equation (23) for $k_y = 0$. By assumption of similar scales, the dispersion relation was decoupled into a solution set seen in Equation (23). Consequently, the quasi-sausage and quasi-kink terms were introduced for the in-phase and anti-phase modes, shortened to sausage and kink for ease of writing.

In Figures 2(a) and (b), we present numerical solutions of Equation (23) for an asymmetric slab system with moderately low plasma-β (0.3), embedded between two environmental regions with different equilibria that are both warmer than the slab itself, with the exact values of the characteristic speeds provided in the figures themselves. Displayed are the normalized phase speeds, $\omega/(k_z v_A)$, given by Equation (23) varied in relation to the magnitude of the product between the vertical component of the wavenumber and dimension of the slab, $k_z x_0$. The ratio of specific heats had a standard value of $\gamma = 5/3$, and the ordering of c_1, c_2, v_A, c_0, c_T (listed in descending order) was kept throughout the process of finding the solutions.

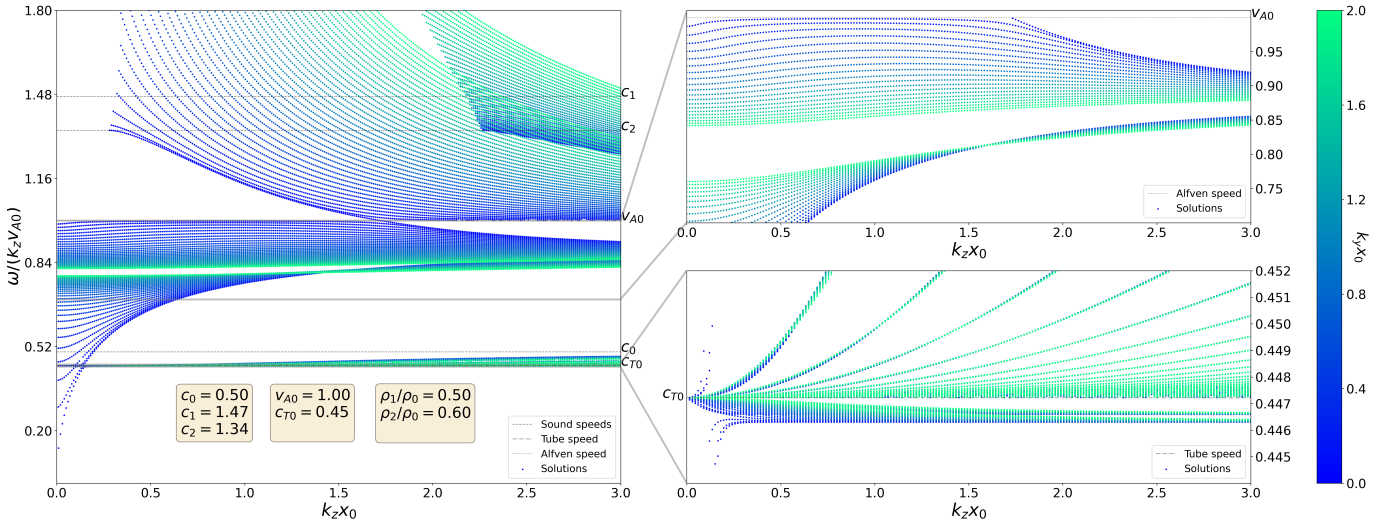

Figure 3. The normalized phase speed of eigenmodes as a function of dimensionless slab width, where the different colors shifting from blue to green indicate the solutions for growing values of the dimensionless slab length $k_y x_0$.

The different modes, where they exist, are plotted with blue. All typical frequencies $k_z c_1$, $k_z c_2$, $k_z v_A$, $k_z c_0$, $k_z c_T$ (listed in descending order) are illustrated in gray with only slight differences in the texture of their line and are shown mainly for reference and comparison, since the spotlight belongs to kc_1, kc_2, ku_+, ku_- (again given in descending order).

For these figures, all speeds were normalized by $k_z v_A$. The lines for kc_1, kc_2, ku_-, and ku_+ are curved as a result, instead of horizontal. In the figures, the normalized versions for these four frequencies are denoted as $\hat{c}_{1,2}$ for $kc_{1,2}/k_z v_A$ and $\hat{u}_\pm$ for $ku_\pm/k_z v_A$, which are depicted in green and red, respectively. The two panels of Figure 2 show solutions in two slabs of different lengths. Both cases show a satisfying degree of similarity to the parallel case, with some new features introduced. Those new observations are more obvious in Figure 2(b) where the contribution of the k_y-component is larger, but are already seen in Figure 2(a) as well, which depicts the solutions found in a very short slab. Further discussion on each individual case is given below. Before that, it must be noted that as $k_z x_0$ increases, and so $k \to k_z$, the curves for u_-, u_+ tend to the minimum and maximum between c_0, v_A, respectively. This was shown analytically in Section 2.6. This also affirms that a wide slab, short or long, will be qualitatively equivalent to the parallel case, which is in turn equivalent to the single-interface case.

To illustrate the increasing role of the contributions from nonparallel propagation, an animated version of Figure 2 is also available, where each step in the animation changes the dimensionless length of the slab, $k_y x_0$, while keeping every other parameter the same. Viewed in conjunction with Figure 3, the increasing deviation from the parallel case can be easily followed and understood (as will be detailed later in Section 4.3).

4.1. Very Short Slab: $\mathrm{k_y d} = 0.05$

While the left-hand-side panel of Figure 2(a) provides an overview of all types of waves and their normalized phase speeds that can propagate obliquely in an asymmetric slab system with the equilibrium parameters listed in the figure, we also provide enlarged versions of certain regions of this diagram. These additional panels, on the right-hand side of Figure 2(a), both help visually discern different modes when they are crowded together in narrow phase-speed bands of the main graph and serve to highlight areas of special interest. The first one of these is the bottom-right panel of Figure 2(a), which shows the slow surface and slow body modes in an enhanced display, while the fast surface and fast body waves are given attention around u_+ in the top-right segment. In further detail, in the bottom-right diagram of Figure 2(a), two slow surface (one quasi-kink, one quasi-sausage) as well as some of the infinite number of slow body modes are seen.

In the thin slab, the slow surface quasi-kink mode does not tend to zero anymore, yet the slow surface quasi-sausage mode tends to c_T, as before. In the wide slab they both tend to a different intermediate speed between 0 and c_T which, for this particular set of parameters, falls quite close to c_T, and they become nearly nondispersive.

The slow body modes are weakly affected by the k_y-component being nonzero and are most similar to the parallel case. Most notably, the phenomenon of a mode that starts out as a slow body wave in a thin slab but transitions into a surface mode (in this case, the fast surface quasi-kink mode) at a small to intermediate slab width is seen again, similarly to the parallel case. As can be seen from Figure 2(a), along with the consecutive frames of its accompanying animation, as well as from the shading in Figure 3, this transition now occurs when the normalized phase speed of the waves is larger than the new classification boundary: $\omega/(k_z v_A) > k\hat{u}_-$. Furthermore, it is clear from these numerical results that the dimensionless length of the slab strongly influences where this transition occurs, with the increase of $k_y x_0$ pushing the transition toward ever thinner slabs.

The rest of the slow body modes still tend to c_T in a thin slab, even in the case of oblique propagation. In a wide slab, however, they approach u_- as the new classification speed. Although this is a physically meaningful difference from the case of purely parallel propagation, it still only appears as a relatively small effect of the nonparallel component, since in a wide slab, as k_z/k increases, it is also true that $u_- \approx c_0$.

The fast surface quasi-sausage mode and the fast body modes are also given further attention in the top-right panel of

Figure 2(a). Their behavior is notably different in the current case of oblique propagation. Namely, in the purely parallel case (reproduced by the first frame of the animated version of Figure 2(a)), there seems to be a continuous transition between the fast body mode descending down toward v_A from higher phase speeds and the fast surface mode appearing at an intermediate slab v_A, to then tend to an intermediate phase-speed value between v_A and c_0 in wide slabs. This speed is different from the one that the fast quasi-kink surface mode tends to. In this respect, the pair of fast surface modes behave similarly here to their slow-mode counterparts.

However, once the propagation is not purely parallel, these two (fast surface and body) waves start showing ever greater separation. The fast quasi-sausage surface mode seems to tend to an intermediate speed between $\hat{u}_-$ and $\hat{u}_+$ in the thin slab, then it tends to u_+ as the slab transitions to a moderately wide one, but finally it tends nearly nondispersively to a different speed in between $\hat{u}_-$ and $\hat{u}_+$ for a wide slab. This behavior could perhaps be explained as an avoided crossing between the fast surface and body modes.

Outside of these interactions with fast surface modes at intermediate slab widths, the fast body modes of all orders tend to $\hat{u}_+$ from above for a wide slab. Although for a thin slab they become leaky solutions, this transition is also dependent on the slab length. In the presence of a nonzero k_y-component, fast body waves with a given phase speed above $\min(c_1, c_2)$, which would have previously been leaky, may still exist as trapped oscillations, so long as they are slower than the new separation limits: $\omega/(k_z v_A) < \min(\hat{c_1}, \hat{c_2})$. Through this effect, the fast body modes are perhaps the ones most spectacularly influenced by the introduction of a k_y-component. Since Figure 2(a) was prepared with a very small nonparallel component of $k_y x_0 = 0.05$, the differences from the parallel case on this graph are weak but already noticeable.

4.2. Short Slab: $\mathrm{k_y d} = 0.15$

To illustrate the increasing influence of the growing $k_y x_0$ value on the dispersion diagrams summarizing oblique wave propagation in an asymmetric slab system, we also included a second snapshot from the animation accompanying Figure 2(a) in the form of Figure 2(b), where now $k_y x_0 = 0.15$. Again, the bottom-right panel of Figure 2(b) displays an enhanced version of the slow surface and slow body modes, along with one fast surface mode, while the top-right panel focuses on the fast surface and fast body modes. The differences from the purely parallel case become more significant, and there are qualitative as well as quantitative differences even between this step and the shorter slab solutions depicted in Figure 2(a).

The slow body modes mostly display the same behavior as before, in a shorter slab, however the wave that changed character from a slow body to a fast surface wave in the very short slab now propagates with a fast enough phase speed so that $\omega/(k_z v_A) > \hat{u}_-$ for any value of $k_z x_0$. This is therefore a surface mode not only in a wide slab, but also in a thin slab already and no longer changes character at an intermediate $k_z x_0$ value. The rest of the fast surface and fast body modes behave similarly to the case illustrated in Figure 2(a), but it is noted that they stay further away from each other around the dividing curve of $\hat{u}_+$. Additionally, as k_y has increased compared to the previous frame, now there is a wider phase-speed band above the lowest external sound speed in which the fast body waves are no longer leaky modes. However, even though their appearance follows the steep $\min(\hat{c_1}, \hat{c_2})$ curve, in a thin slab they still cannot be found as trapped oscillations. In slabs that are already wide, the effect of lengthening the slab is smaller on these modes, as the gradients of both curves bounding the band of fast body modes ($\min(\hat{c_1}, \hat{c_2})$ and $\hat{u}_+$) are much smaller at large $k_z x_0$ values.

4.3. Visualizing the $\mathrm{k_y}$ Variation

In order to make comparisons between short and long slabs easier and point out further practical consequences of incorporating nonparallel propagation into slab models of the solar atmosphere, on top of the animation accompanying Figure 2, we also include a different approach to portraying the propagating modes in the form of Figure 3. This new approach includes all past features from Figure 2, but also merges the separate frames from different values of k_y into one diagram. The difference in slab length is portrayed with a color gradient, also indicated by a bar on the right of the figure. Specifically, as $k_y x_0$ increases, the color of the solution curves changes from dark blue to light blue and eventually into teal/green colors. We only indicate the original sound speeds (c_0, c_1, c_2), Alfvén speed (v_A), and tube speed (c_T) on this figure. The new classification ($\hat{u}_\pm$) and separation limits ($\hat{c_1}$, $\hat{c_2}$) were omitted to avoid visual confusion, as they would also keep changing with the increasing k_y-component and overlap with the plotted solutions. They are still the relevant speeds separating body and surface, or trapped and leaky modes, but where they fall in each case is more easily followed in the animation attached to Figure 2.

This visualization of the solutions provided in Figure 3 highlights further interesting consequences of allowing varying degrees of oblique propagation to take place in the asymmetric slab system. Focusing first on the left-hand-side panel of Figure 3 and looking at the fast body modes (with $1 \leqslant \hat{u}_+ < \omega/(k_z v_A) < \min(\hat{c_1}, \hat{c_2})$ at relatively large slab widths, $k_z x_0 > 1.5$), an overlap can be found between the first and second solution curves in the set of infinite body modes as k_y is changed. This overlap could occur between quasi-kink and quasi-sausage modes of the same order, that is, with the same number of nodes inside the slab, or between body modes of order n and $n + 1$. This phenomenon highlights the importance of collecting detailed information about the character of waves observed in the solar atmosphere, including the distribution of displacement and pressure perturbation throughout the slab system for discerning between (quasi-) kink and (quasi-) sausage modes, and for correctly identifying the order of a given body mode. In the lack of such spatial information, if for example a wave with a normalized phase speed of roughly $1.2 < \omega/(k_z v_A) < 1.6$ were detected in a system with a dimensionless slab width of $2 < k_z x_0$ (which would fall somewhere in the green-blue overlap region on Figure 3), it could be either one of the two modes propagating in this region of the parameter space, depending on whether there is a k_y-component to its propagation or it happens in a purely parallel manner.

In order to investigate whether a similar phenomenon can occur when the oblique propagation of other modes is allowed, we studied the other regions of interest further, and include these results in the right-hand-side panels of Figure 3. First, the bottom-right panel shows the solutions at various slab lengths and widths which propagate with a phase speed close to the internal tube speed. The waves with $0 < v_{ph} < c_T$ are the slow

surface quasi-kink and quasi-sausage mode solutions. At smaller slab widths (up to approximately $k_z x_0 = 1.5$ in this case), this type of quasi-sausage mode propagating with a smaller k_y-component could have a similar phase speed to a quasi-kink mode propagating more obliquely—therefore, once again, when it comes to observations for SMS purposes, the collection of detailed spatial information is crucial to distinguish between these solutions.

While the slow body modes ($c_{T0} < \omega/(k_z v_A) < \hat{u}_- \leqslant c_0$) do not show a similar overlaps, another interesting influence of the angle of propagation can be observed in their case. The phase speeds of all of the other types of modes (slow surface and fast body modes) described so far shift in one direction only across the whole range of investigated slab widths examined as an increasing k_y-component is introduced into their propagation. However, the phase speeds of each order of slow body modes increase thin slabs as k_y increases, but in wide slabs the phase speeds decrease instead. Thus, at a certain slab width (which is different for each order of body mode), the phase speeds of slow body modes propagating at different angles end up being nearly identical (see the points on the bottom-right panel of Figure 3 where the solutions plotted with blue and green colors swap places). These areas of the dispersion diagram are, once again, regions where collecting exact information on the direction of propagation is extremely important when carrying out SMS studies. Without knowing the relative magnitudes of the k_y- and k_z-components of the wavenumber vector, essentially the same phase speed could belong to any number of slow body modes of the same order, which then would introduce an additional source of uncertainty in the parameters an SMS study aimed to measure (such as the Alfvén speed or the magnetic field strength).

Finally, the top-right panel of Figure 3 focuses on the fast surface modes ($\hat{u}_- < \omega/(k_z v_A) < \hat{u}_+$). Unlike their slow-mode counterparts, these do not show overlap regions between the quasi-sausage and the quasi-kink modes either. However, while the phase speed of the quasi-sausage modes consistently becomes smaller as k_y increases across the entirety of the slab width range examined, the phase speed of the quasi-kink modes has a turning point—similar to the case of slow body modes. This behavior seems to be consistent with the fact that, at least for small slab lengths, this mode starts out in the same phase-speed band as the slow body modes in a thin slab, and it crosses the classification threshold ($\hat{u}_-$) to the surface mode band only at some intermediate slab width. Consequently, the significance of collecting appropriate information on the direction of wave propagation that we emphasized with slow body modes also extends to this surface mode.

5. Discussion

Presented above is a novel model of an isolated magnetic slab, with an asymmetric environment and nonparallel wave propagation considered. This is an expansion on the "classical" magnetic slab models seen in the past (B. Roberts 1981b) in two respects. Similarly to the more recent model developed by M. Allcock & R. Erdélyi (2017), it considers an asymmetric configuration, but, further expanding upon the asymmetric model itself, it allows for the oblique propagation of MHD waves in the slab. The main focus of this paper is on the consequences of an oblique wavevector regarding the properties of the different propagating modes by deriving the dispersion relation applicable to the system and carrying out an analytical and numerical study of the solutions.

Before we move to the differences between the eigenmodes of the system studied here and the symmetric slab models, we note that the sausage and kink modes are modified by the asymmetry of the external regions, resulting in the presence of the quasi-sausage and quasi-kink modes. These modes were already studied by M. Allcock & R. Erdélyi (2017) and, as the nonparallel condition does not affect this change, they have appeared as seen in the parallel, asymmetric model and so have remained unchanged.

Now, a property of the system that is greatly affected by the nonzero k_y-component in our model is the boundaries of the intervals of propagation of the dispersion relation and the classification into surface and body modes. In the models of parallel propagation, the three important such boundaries are the tube, sound, and Alfvén speeds. Here, however, the role of the latter two is taken by u_- and u_+, which have appeared in conjunction with the full wavenumber vector $\boldsymbol{k}$ rather than only the parallel component, k_z.

These new speeds emerge when replacing m_0, the wavenumber-like coefficient appearing in the ODE that governs the behavior of perturbations in the slab, with μ_0, which as a modified version of this quantity simply accounts for the presence of the k_y-component on top of the information about the waves and the background contained in m_0. As a result, the classification of waves into body and surface modes is now determined by the frequency limits $k_z c_T$, ku_-, and ku_+. These limits have a fixed ordering, removing one concern when considering wave propagation. On the other hand, the latter two are k_y dependent, which is perhaps one of the most interesting results from this model of oblique propagation.

The role of the k_y-component, as it appears in these quantities contributing to the dispersion relation, implies that for the same width of the slab and for the same scale of frequency, modes can change from surface to body waves by simply turning the wavenumber vector away from the lateral axis.

Another consequence of these new velocities determining classification is that $\omega^2 = k_z^2 c_0^2$ and $\omega^2 = k_z^2 v_A^2$ are no longer spurious solutions and are permissible frequencies, as long as k_y is nonzero. When k_y is zero, then the new frequencies ku_- and ku_+ reduce to $k_z \min(c_0, v_A)$ and $k_z \max(c_0, v_A)$ as expected.

When it comes to numerical approximations, we are pleased to report a satisfying match between the analytical and numerical results. Under the respective conditions—incompressible, low-β, thin or wide, short or long—the analytical approximations derived in Section 3 show a good correspondence with all approximations that were tested, with some illustrative examples included in the Appendix.

Besides the predicted behavior studied in Section 3, the region between fast surface and fast body modes has offered some alluring outcomes. Specifically, a very important mode from the parallel propagation case, which has been seen to change character between a fast surface and a fast body wave, is now observed to split into two separate modes. Those two, instead of blending from one into the other, now show an avoided crossing as a nonzero k_y-component is incorporated. This separation happens around the same slab width where the shift in character took place in the case of parallel propagation, and becomes only more prominent as k_y increases.

A further noteworthy finding of our study concerns the applications of theoretical MHD wave studies like the current one. When using slab models for the purposes of solar magneto-seismology, as mentioned earlier, the aim is to utilize the measured background parameters of the slab system and the observed wave properties to draw conclusions about "missing" background parameters with the help of the analytical expressions derived for each model. Our results, especially as they appear illustrated for a given set of plasma and magnetic parameters in Figure 3, highlight the importance of collecting not only temporal information about the waves (frequency/period), but also spatial information (including energy distribution, wavelength, as well as the direction of propagation) for the purposes of mode identification, which in turn will influence the final results obtained for the background parameters left to determine. The effect of the propagation angle on the speed and identification of the eigenmodes of a slab system is applicable in the case of fast body modes which occupy a large region of the parameter space.

Beyond the results explored in this paper, the study of oblique propagation in slab models is also a promising area for future research. With the inclusion and variation of the k_y-component, layered and multilayered Cartesian structures can now develop greater variance in topology and application. A series of recent studies analyzed the parallel propagation problem in various asymmetric configurations, from single slabs with different atmospheric, bulk fluid, and magnetic properties (P. M. Edwin & B. Roberts 1982; N. K. Zsámberger et al. 2018, 2022; D. Shukhobodskaia & R. Erdélyi 2018; M. Allcock et al. 2019; N. K. Zsámberger & R. Erdélyi 2020).

For a more complete understanding and wider applicability of MHD wave propagation investigated in Cartesian systems, any of the models referenced above can be revisited to include a nonparallel component, leading to an enhanced understanding of their suggested solar applications, too. These applications can be divided into two main types: global and local seismological studies. The category of global applications involves investigating the layers of the solar atmosphere as asymmetric slab systems, for example looking at wave propagation in a slice, the transition region as a slab, surrounded by the different environmental regions of the corona and the chromosphere from above and below. In addition to this, a growing list of local applications has been proposed (for a summary, see the recent review by R. Erdélyi & N. K. Zsámberger 2024). Out of these, it would be especially interesting to utilize our updated slab model to study nonparallel wave propagation in prominences, light bridges, or magnetic bright points (MBPs). These features of the solar atmosphere can be handled as asymmetric slab systems in a first approximation as they can have a significantly larger extent in one spatial direction perpendicular to the magnetic field (the z-direction in our notation), marking this as the y-direction in our model. Each of these structures furthermore is embedded between different, easily separated regions of the solar atmosphere. Prominences are held up by magnetic fields between different coronal layers. Light bridges occur between separate umbral cores as sunspots merge or split. MBPs show up in the dark intergranular lanes, wedged in between two different cells of the solar granulation. Taking into consideration the infinite versus finite length of slabs, studies of propagating and standing waves can both be carried out with small changes to the model described in the current paper. This could also be an insightful approach to dealing with barriers that encircle and/or separate dynamic, magnetic entities in the solar atmosphere, such as barriers of coronal holes and sunspots.

Acknowledgments

R.E. is grateful to the Science and Technology Facilities Council (STFC, UK), grant No. ST/M000826/1, and acknowledges NKFIH (OTKA, grant No. K142987 and Excellence Grant, grant No. TKP2021-NKTA-64) Hungary and PIFI (China, grant No. 2024PVA0043) for enabling this research. This work was also supported by the International Space Science Institute project (ISSI-BJ ID 24-604) on "Small-scale eruptions in the Sun." N.Z. and R.E. are further thankful for the support received from STFC (UK) under grant No. ST/V003712/1. N.Z. and A.T. are also grateful for the support received from the SURE scheme at the University of Sheffield, which enabled the initiation of this research. B.A. thanks the DKÖP-2023 grant of the Ministry of Culture and Innovation, Hungary for making this research possible. This work was also supported by the EKÖP-KDP-24 University Excellence Scholarship Program Cooperative Doctoral Program of the Ministry for Culture and Innovation from the source of the National Research, Development and Innovation Fund.

Appendix A
Amplitudes

In addition to the discussion about the dispersion relation and its solutions, we also carried out a brief investigation of the spatial structure of the different obliquely propagating waves. Our main conclusions on this agree with the results presented in the studies of different slab systems where a nonparallel component of wave propagation was also allowed, such as A. J. Díaz et al. (2003) and I. Arregui et al. (2007). Namely, the inclusion of a k_y-component leads to steeper exponential drop-off rates of the transverse velocity amplitude ($\hat{v_x}$) in the environment of the slab, as also shown in the case of the illustrative example of surface modes that we included in Figure 4.

However, we also note an additional effect related to the asymmetry of the slab geometry studied here: the magnitude of k_y also displays additional influence over the values that the eigenfunctions take at the slab boundaries. The velocity amplitudes at the boundaries of the slab are already different from each other for all asymmetric eigenmodes even without the inclusion of a k_y-component (see, e.g., M. Allcock et al. 2019; R. Erdélyi & N. K. Zsámberger 2024), but these values are further shifted by the inclusion of an increasingly oblique direction of propagation. While in the explored parameter range this effect always acts to increase the asymmetry of the amplitudes at the boundaries, this may be accomplished in various ways. For example, in Figure 4(a), as the k_y-component grows through the plotted cases (that is, moving from the blue to the red and finally to the green continuous curve) for the quasi-kink modes of growing obliqueness, the amplitudes at both boundaries are decreased by different amounts (so that the overall relative asymmetry between them still grows). The opposite is true for the quasi-sausage modes plotted with dashed lines in the same figure: As k_y grows (from the blue to the green curve), the amplitudes at the two boundaries are shifted in opposite directions, which leads to a

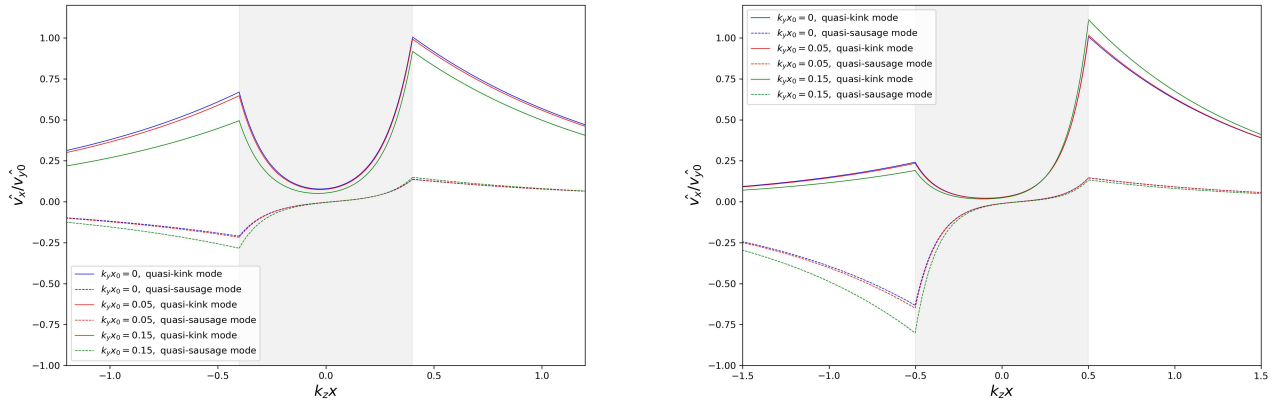

(a) $k_z x_0 = 0.4$ (b) $k_z x_0 = 0.5$

Figure 4. Eigenmodes for 0.36% asymmetry in densities ($\rho_1/\rho_0 = 0.5$, $\rho_2/\rho_0 = 0.5018$) for two slab widths. Increasing $k_y x_0$ in the transverse direction causes increasing asymmetry in the eigenmode amplitudes, and it also increases the drop-off rate of the eigenmodes on both sides of the slab by 4.8% between $k_y x_0 = 0$ and $k_y x_0 = 0.15$ for the slab width $k_z x_0 = 0.5$ (7.4% for $k_z x_0 = 0.4$). The physical parameters for the systems are $c_0 = 0.5$, $c_1 = 1.47196$, $c_2 = 1.46932$, and $v_{A0} = 1.0$, with $k_z x_0$ values indicated under the figures.

more easily visible increase in the relative amplitude difference.

The situation becomes different for the case of a slightly wider slab, as illustrated in Figure 4(b). Here, it is the quasi-kink modes (plotted with continuous lines) that have their maximum amplitudes at the boundaries of the slab shifted in different directions as k_y increases. On the other hand, the amplitudes at the boundaries for the quasi-sausage modes (plotted with dashed lines) in this thicker slab are shifted in opposite directions.

Appendix B
Approximations

To examine the behavior and accuracy of our analytical solutions to the dispersion relation (gathered in Section 3), here we illustrate them overlaid with the exact, numerically found solutions to the dispersion relation.

The depicted frequencies are normalized by $k_z v_A$. In faded gray, we have the normalized classification frequencies $k_z c_1$, $k_z c_2$, $k_z v_A$, $k_z c_0$, $k_z c_T$, and in green the separation frequencies kc_1, kc_2 normalized to $\hat{c}_{1,2}$. Additionally, the curves for the classification frequencies, $ku_\pm$, are drawn in red and are also normalized by $k_z v_A$. The modes emerging from the full dispersion Equation (23) are seen in blue, while the analytical solutions from the equations of Section 3 are seen in orange. Finally, to distinguish the various analytical solutions, we introduce a naming scheme using ω with a subscript of the equation number the curve emerges from, e.g., the curve labeled ω_{43} is a representation of the approximate solution described by Equation (43). As different solutions can occur in slabs with different internal plasma-β parameters, and in some small regions of normalized phase speeds there is a wealth of different modes to be found, we break down our comparison into three separate figures. First, Figure 5 shows analytical and numerical solutions in a slab characterized by $\beta = 0.3$, which can go from thin to wide as well as short to long. Figure 6 focuses on only thin and short slabs of the same $\beta = 0.3$ case. Finally, Figure 7 shows the solutions in thin and short slabs with $\beta = 0.12$. A complete breakdown of the naming scheme of the solution curves also follows:

1. ω_{43} := slow surface quasi-sausage modes in a thin-short slab (Figure 6).
2. ω_{44} := fast surface quasi-sausage modes in a thin-short slab (Figure 7).
3. ω_{45} := slow surface quasi-kink modes in a thin-short slab (Figure 6).
4. ω_{46} := slow quasi-sausage body modes in a thin-short slab (Figure 6).
5. ω_{47} := slow quasi-kink body modes in a thin-short slab (Figure 6).
6. ω_{49} := slow quasi-sausage body modes in a wide and/or long slab (Figure 5).
7. ω_{50} := slow quasi-kink body modes in a wide and/or long slab (Figure 5).
8. ω_{51} := fast quasi-sausage body modes in a wide and/or long slab (Figure 5).
9. ω_{52} := fast quasi-kink body modes in a wide and/or long slab (Figure 5).

Note that the figures in this appendix overall showcase solutions in different analytical limits, therefore not all regions in each figure show a close correspondence with the exact solutions. For example, in Figure 5, the wide-long slab approximation for slow body modes follows the numerical solutions when $k_z x_0 > 6$ in our still image with $k_y x_0 = 1$. The approximations work better for a larger range of $k_z x_0$ when the slab becomes longer, which is shown in the steps of the animated version of our figure. The approximations for fast body modes in this same figure and the attached animation however at least qualitatively follow the gradient of the solution curves in the entire $k_z x_0$ region displayed here.

The opposite tendency is observable in Figure 6, where all approximations, both for slow body and surface modes, show a close correspondence with the exact solutions when $k_z x_0 < 0.1$. This boundary shifts to even lower slab widths as $k_y x_0$ increases in the animated version of this figure. This behavior is not unexpected, as the approximations plotted here were derived for thin and short slabs, and they can start to break down when either dimension of the slab is increased too much compared to the typical wavelengths of perturbations.

Finally, in Figure 7, we illustrate a case slightly different from the rest, with a lower plasma-β of 0.1, which allows us to compare our approximation provided in Equation (44) to the

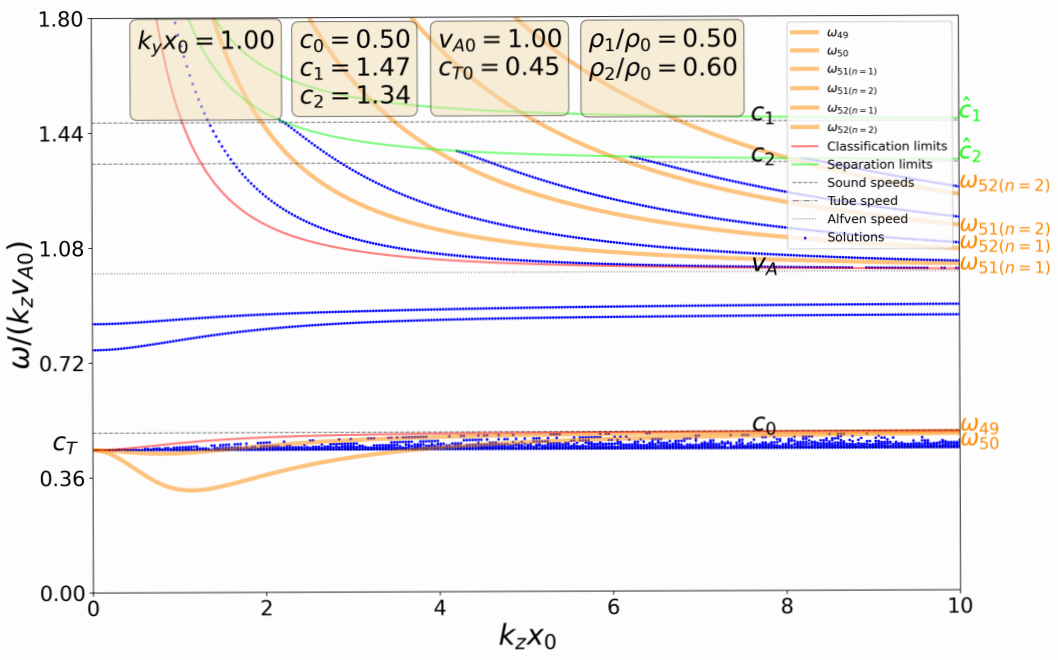

Figure 5. A comparison of solutions to the full dispersion relation (Equation (23)) and the analytical solutions given in the limits studied in Section 3, with an asymmetric waveguide showing the wide slab phenomena. For a complete breakdown of the naming conventions, see text in Appendix B. An animation accompanying this figure is available, where each frame increases slab length $k_y x_0$ by 0.1 between $k_y x_0 = 0.0$ and $k_y x_0 = 4.0$ while keeping all other parameters intact. They show the evolution of analytical approximations in comparison to the numerical solutions to the full dispersion relation in relation to the also changing separation limit.

(An animation of this figure is available in the online article.)

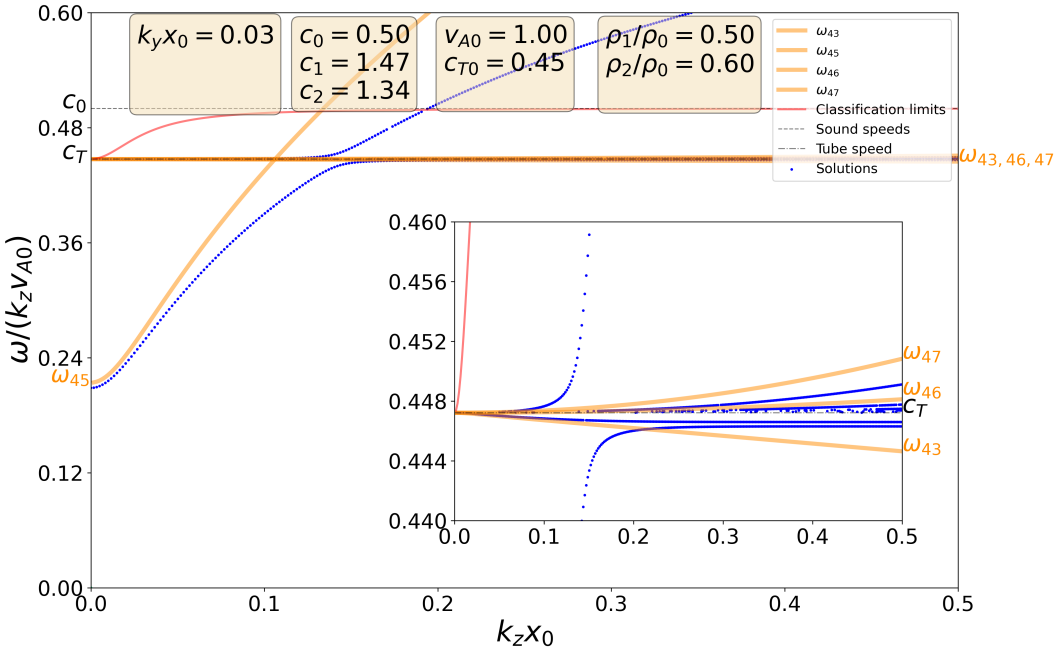

Figure 6. A comparison of solutions to the full dispersion relation (Equation (23)) and the analytical solutions given in the limits studied in Section 3, with an asymmetric waveguide showing the behavior of analytical solutions in the thin-short slab region, focusing on the slow modes. For a complete breakdown of the naming conventions, see text in Appendix B. An animation accompanying this figure is available, where each frame increases slab length $k_y x_0$ by 0.025 between $k_y x_0 = 0.0$ and $k_y x_0 = 0.5$ while keeping all other parameters intact. The inlet enlarges the very small range of normalized phase speeds around the internal tube speed to show the narrow band of slow body mode solutions there.

(An animation of this figure is available in the online article.)

exact fast surface quasi-sausage mode solutions. In the animation accompanying this image, it becomes apparent that in systems with an increasing slab length, even for thin slabs, there is a marked difference between the approximation scaling with the separation speed related to $\hat{c_e}$ and the full solutions, which start tending to an intermediate speed

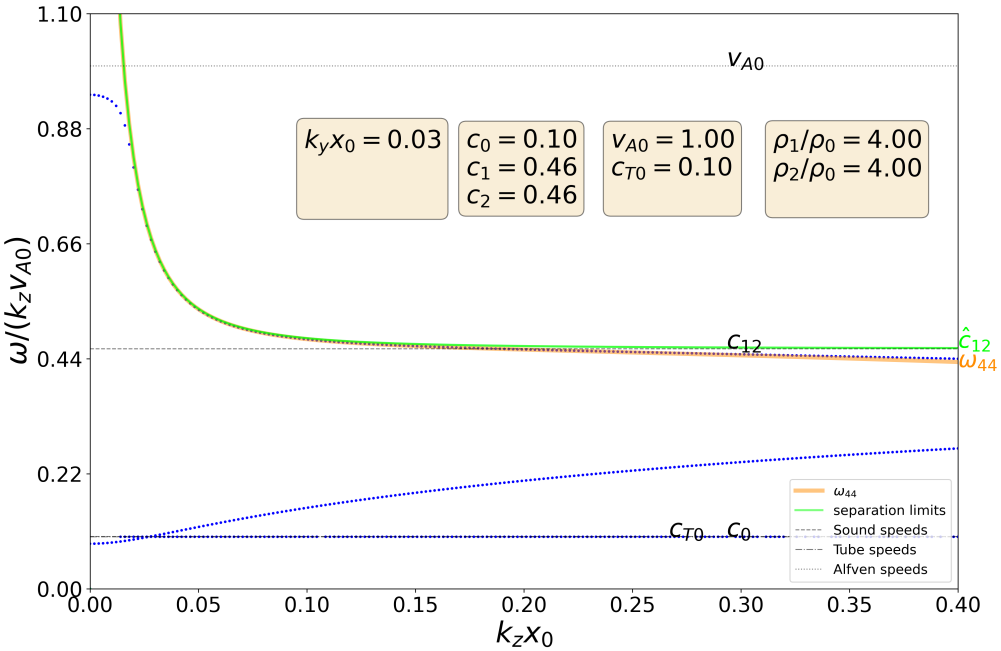

Figure 7. A comparison of solutions to the full dispersion relation (Equation (23)) and the analytical solution given in the limits studied in Section 3, with a symmetric waveguide and lower plasma-β. For a complete breakdown of the naming conventions, see text in Appendix B. An animation accompanying this figure is available, where each frame increases slab length $k_y x_0$ by 0.01 between $k_y x_0 = 0.0$ and $k_y x_0 = 0.1$ while keeping all other parameters intact.
(An animation of this figure is available in the online article.)

between it and u_-. Overall, Figures 5–7 make it clear that even if some approximations, like the one describing the slow body modes, start very far from the full solutions of the desired mode in a certain range of slab length and width, for the range where the approximations are expected to be valid the two curves match up well. In some cases, like the fast body modes, the agreement between the exact and the approximate solutions remains good even in a much larger range of slab width and length parameters than expected.

ORCID iDs

Antreas Tsiapalis https://orcid.org/0009-0000-9782-0651
Noémi Kinga Zsámberger https://orcid.org/0000-0002-2822-129X
Balázs Asztalos https://orcid.org/0000-0001-8530-5855
Robert Erdélyi https://orcid.org/0000-0003-3439-4127

References

Allcock, M., & Erdélyi, R. 2017, SoPh, 292, 35
Allcock, M., & Erdélyi, R. 2018, ApJ, 855, 90
Allcock, M., Shukhobodskaia, D., Zsámberger, N. K., & Erdélyi, R. 2019, FrASS, 6, 48
Andries, J., van Doorsselaere, T., Roberts, B., et al. 2009, SSRv, 149, 3
Arregui, I., & Ballester, J. L. 2011, SSRv, 158, 169
Arregui, I., Ballester, J. L., Oliver, R., Soler, R., & Terradas, J. 2012, in ASP Conf. 455, 4th Hinode Science Meeting: Unsolved Problems and Recent Insights, ed. L. Bellot Rubio, F. Reale, & M. Carlsson (San Francisco, CA: ASP), 211
Arregui, I., Terradas, J., Oliver, R., & Ballester, J. L. 2007, SoPh, 246, 213
Aschwanden, M. J., Fletcher, L., Schrijver, C. J., & Alexander, D. 1999, ApJ, 520, 880
Banerjee, D., Erdélyi, R., Oliver, R., & O'Shea, E. 2007, SoPh, 246, 3
Banerjee, D., Krishna Prasad, S., Pant, V., et al. 2021, SSRv, 217, 76
Barbulescu, M., & Erdélyi, R. 2018, SoPh, 293, 86
De Moortel, I., & Nakariakov, V. M. 2012, RSPTA, 370, 3193
Díaz, A. J., Oliver, R., & Ballester, J. L. 2003, A&A, 402, 781
Edwin, P. M., & Roberts, B. 1982, SoPh, 76, 239
Erdélyi, R., & Taroyan, Y. 2008, A&A, 489, L49
Erdélyi, R., & Zsámberger, N. K. 2024, Symm, 16, 1228
Goossens, M., Andries, J., & Aschwanden, M. J. 2002, A&A, 394, L39
Goossens, M., Erdélyi, R., & Ruderman, M. S. 2011, SSRv, 158, 289
Heyvaerts, J., & Priest, E. R. 1983, A&A, 117, 220
Joarder, P. S., & Roberts, B. 1992a, A&A, 256, 264
Joarder, P. S., & Roberts, B. 1992b, A&A, 261, 625
Joarder, P. S., & Roberts, B. 1993, A&A, 277, 225
Komm, R., De Moortel, I., Fan, Y., Ilonidis, S., & Steiner, O. 2015, SSRv, 196, 167
Mathioudakis, M., Jess, D. B., & Erdélyi, R. 2013, SSRv, 175, 1
McLaughlin, J. A., Hood, A. W., & de Moortel, I. 2011, SSRv, 158, 205
Morton, R. J., Verth, G., Jess, D. B., et al. 2012, NatCo, 3, 1315
Nakariakov, V. M., & Ofman, L. 2001, A&A, 372, L53
Nakariakov, V. M., Ofman, L., Deluca, E. E., Roberts, B., & Davila, J. M. 1999, Sci, 285, 862
Nakariakov, V. M., & Roberts, B. 1995, SoPh, 159, 213
Nakariakov, V. M., & Verwichte, E. 2005, LRSP, 2, 3
Nakariakov, V. M., Zhong, S., Kolotkov, D. Y., et al. 2024, RvMPP, 8, 19
Roberts, B. 1981a, SoPh, 69, 27
Roberts, B. 1981b, SoPh, 69, 39
Roberts, B. 2024, SoPh, 299, 76
Roberts, B., Edwin, P. M., & Benz, A. O. 1984, ApJ, 279, 857
Rosenberg, H. 1970, A&A, 9, 159
Ruderman, M. S., & Erdélyi, R. 2009, SSRv, 149, 199
Shukhobodskaia, D., & Erdélyi, R. 2018, ApJ, 868, 128
Uchida, Y. 1970, PASJ, 22, 341
Wang, T. 2011, SSRv, 158, 397
Zajtsev, V. V., & Stepanov, A. V. 1975, IGAFS, 37, 3
Zsámberger, N. K., Allcock, M., & Erdélyi, R. 2018, ApJ, 853, 136
Zsámberger, N. K., & Erdélyi, R. 2020, ApJ, 894, 123
Zsámberger, N. K., Tong, Y., Asztalos, B., & Erdélyi, R. 2022, ApJ, 935, 41